nature communications

Article

https://doi.org/10.1038/s41467-025-60186-6

High-entropy-doping effect in a rapid-charging Nb_2O_5 lithium-ion battery negative electrode

Received: 17 October 2024

Accepted: 14 May 2025

Published online: 29 May 2025

Check for updates

Junling Xu[1,9] ✉, Fuqiang Xie[1,9], Lipeng Huang[1], Nana Li[2], Shang Peng[2], Wensheng Ma[3], Kai Zhang[2], Yanxue Wu[4], Lianyi Shao[1], Xiaoyan Shi[1], Jizhang Chen[5], Li Tao[6], Kai Zhang[7], Zhonghua Zhang[3], Yonggang Wang[8] ✉ & Zhipeng Sun[1] ✉

Doping is an important approach to tailor materials' properties, yet the success of doping can depend on factors such as ionic radii similarities. For materials like silicon or perovskite, doping is not only facile to implement but can also enhance material properties. However, for host lattice structures like Nb_2O_5, doping without causing phase change is challenging. Here, we introduce a high-entropy-doping effect in Nb_2O_5. Unlike traditional doping approaches, high-entropy-doping minimizes the chemical properties of doping elements and focuses solely on their quantities. By high-entropizing the doping elements (selecting 10–15 from Mg, Ca, Sr, Ba, Cr, Mn, Fe, Co, Ni, Cu, Zn, Al, Ga, In, Sn, Sb, Y, Mo, La, Ce) and keeping them within a certain range of doping concentrations (1–3 $_{mol}$%), a successful high-entropy-doping is achieved for Nb_2O_5 without phase change. The obtained high-entropy-doped (HED) Nb_2O_5 exhibits rapid-charging capabilities. At a rate of 40 A g^{-1}, the HED-Nb_2O_5 delivers a capacity of 80 mAh g^{-1}, whereas the undoped Nb_2O_5 fails to exceed 25 mAh g^{-1}.

The phenomenon of doping in solids has long been the research subject in the field of materials science. Doping has been widely validated for its ability to enhance solid properties across various material systems. For instance, doping phosphorus and boron into intrinsic silicon semiconductor materials substantially enhances their conductivity, resulting in respectively enhanced electron-type and hole-type semiconductors[1]. Incorporating small amounts of iron into titanium alloys using additive manufacturing methods creates an alloy with high strength and improved ductility[2]. Rare-earth-doped nanoparticles shorten the luminescence decay to sub-50 ns while maintaining high quantum efficiency enhancement[3]. The ion migration in metal halide perovskites can be suppressed by doping multivalent cations[4,5]. Doping is relatively straightforward to promote the properties of these materials. Especially, for materials like perovskites or layered metal oxides, the dopant even becomes completely miscible within the material being doped, also resulting in significant

[1]School of Materials and Energy, Guangdong University of Technology, Guangzhou, China. [2]Center for High Pressure Science and Technology Advanced Research (HPSTAR), Shanghai, China. [3]School of Materials Science and Engineering, Shandong University, Jinan, China. [4]Analysis and Test Center, Guangdong University of Technology, Guangzhou, China. [5]Co-Innovation Center of Efficient Processing and Utilization of Forest Resources, College of Materials Science and Engineering, Nanjing Forestry University, Nanjing, China. [6]Key Lab of Advanced Optoelectronic Quantum Architecture and Measurement (Ministry of Education), School of Physics, Beijing Institute of Technology, Beijing, China. [7]Frontiers Science Center for New Organic Matter, Renewable Energy Conversion and Storage Center (RECAST), Key Laboratory of Advanced Energy Materials Chemistry (Ministry of Education), College of Chemistry, Nankai University, Tianjin, China. [8]Department of Chemistry and Shanghai Key Laboratory of Molecular Catalysis and Innovative Materials, Institute of New Energy, iChEM (Collaborative Innovation Center of Chemistry for Energy Materials), Fudan University, Shanghai, China. [9]These authors contributed equally: Junling Xu, Fuqiang Xie. ✉e-mail: jlxu@gdut.edu.cn; ygwang@fudan.edu.cn; zpsunxj@gdut.edu.cn

improvement in properties[5,6]. However, for particular materials and their corresponding dopants, successful doping in the lattice is difficult. This implies that doping within these materials introduces impurity phases or cause a phase transformation. For instance, in the Wadsley-Roth type Nb_2O_5[7–12], a rapid-charging negative electrode material for lithium-ion batteries, doping with metallic elements present notable changes in the lattice. The dopant species generally induce phase transitions forming new shear phase or two-dimensional phase within Nb_2O_5. When utilizing nickel or zinc ions for doping, Nb_2O_5 would change to new phases, such as Wadsley-Roth structured nickel niobate with new shear phase or zinc niobate with a two-dimensional planar structure[13–15]. This reveals the infeasibility of conventional doping approaches for Nb_2O_5.

The emergence of phase transitions or the formation of new phases caused by doping can find theoretical foundations in classical phase transition theories. According to Landau's phase transition theory[16], transitions between crystals and liquids, or between crystals with varying symmetries, involve the appearance or disappearance of specific symmetry elements. The appearance of new phases or impurity phases caused by doping also signifies the phenomenon of symmetry breaking in the original phase system under doping-induced perturbations. In a 1972 paper "More is Different"[17], Philip Anderson pointed out that novel properties emerge at every level of complexity. This "More is Different" phenomenon may also exist in materials doping, theoretically. As Boltzmann noted, the essence of entropy lies in the total number of microscopic configurations corresponding to a macroscopic state. Therefore, by increasing the variety of doping elements, we inevitably induce an impact on the system's number of states. Based on this, we define the doping method that increases the number of doping elements as "high-entropy-doping", and the resulting changes in system properties as the "high-entropy-doping effect".

Nb_2O_5 is an oxide with complex phase transition behavior and high-valence cations, making it extremely challenging to form solid solutions. Ordinary doping methods often introduce impurities, while successful high-entropy-doping impacts the system's microscopic configurational states, making Nb_2O_5 an ideal choice for our study. At the same time, it is important to note that the concept of high-entropy materials has already been widely applied and extensively studied in the field of materials research. High-entropy materials are defined as solid solution phases formed by mixing five or more elements in nearly equimolar ratios. This concept originated in metallic materials[18,19], but now many materials, such as oxides with a rock-salt structure, can also be prepared as high-entropy materials[20–23]. However, there are significant differences between our research on high-entropy-doping Nb_2O_5 and previous studies on high-entropy materials. On the experimental operation, previous studies about high-entropy materials tended to select elements with specific properties and preferred lattices that easily form solid solution. In contrast, our research strives to select elements of different types without strict selectivity, and we tend to choose matrices that are prone to phase transitions. On the theory of thermodynamic statistics, previous studies[23] about high-entropy materials described the number (Ω) of microscopic states in a system as: $\Omega = N!/\prod_i n_i!$, where $N = \sum_i n_i$, N refers to the total number of elements and n_i refers to the number of element i. Using Stirling's approximation, the configurational entropy (S_{conf}) can be expressed as: $S_{conf} = R\sum_i x_i \ln x_i$, where $x_i = n_i/N$ and R refers to is the universal gas constant. In this framework, the configurational entropy can be easily calculated and obviously, this configurational entropy is maximized when the elements are found in equiatomic proportions. However, we argue that this description applies only to ideal cases. In real systems, when external disturbances are introduced, the configurational value N evolves into $N \pm C$, where C refers to the new crystallographic sites caused by new types of atoms, which substantially alters microscopic states. If the universality of these new sites is disregarded, the relationship $N = \sum_i n_i$ should remain unchanged. Under these conditions, the number of microscopic states becomes: $\Omega = (N \pm C)!/\prod_i n_i!$, making the configurational entropy $S_{conf} = k_B \ln \Omega$ difficult to compute, where k_B refers to Boltzmann constant.

Actually, for the complex doping, Zhang et al. have explored a doping strategy in easily doped zero-cobalt layered oxides[24]. Although the type number of doping elements was limited to four, they still succeeded in creating a highly stable layered positive electrode material exhibiting zero strain characteristics. However, the significance and impact of complex doping (high-entropy-doping) extend beyond altering the characteristics of the base material solely based on the chemical properties of the doping elements. To some extent, the effectiveness of the high-entropy-doping might be contingent more upon the quantity of element types rather than the inherent chemical properties of the individual elements. By high-entropizing the doping elements, the complexity of the system heightens, facilitating effective bridging of the symmetry-breaking gaps.

In this work, we validate this principle using a rapid-charging Nb_2O_5 lithium-ion negative electrode, which is inherently difficult to dope. Through the inclusion of a diversity of doping elements, we successfully achieve high-entropy-doping for this intricate material within a certain range of doping concentrations. We term this phenomenon the high-entropy-doping effect. Besides, the resulting HED-Nb_2O_5 exhibits an enhanced rate capability compared to undoped Nb_2O_5.

Results

Observation of high-entropy-doping effect in Nb_2O_5

Nb_2O_5 typically undergoes phase transitions initially from TT-phase to T-phase, then to M-phase, and finally to H-phase as temperature increases[25,26], where M-phase is metastable and difficult to be obtained if annealed in air. Thus, the annealing atmosphere generally affects this phase transition pathway substantially. As illustrated in Fig. 1a, in an air atmosphere, T-Nb_2O_5 (PDF#−30-0873) transforms into H-Nb_2O_5 (PDF#−37-1468) between 900 °C and 950 °C. However, if in an inert gas environment (Fig. 1b), T-Nb_2O_5 partially transforms into M-Nb_2O_5 (PDF#−32-0711) between 850 °C and 900 °C until it fully converts into M-Nb_2O_5 at 950 °C. Oxygen vacancies of the M-phase formed in inert atmosphere are regarded to stabilize its metastable crystal structure. With further temperature increases, M-Nb_2O_5 continues to convert into H-Nb_2O_5. X-ray diffraction (XRD) patterns indicate that the M-phase has fewer diffraction peaks than the H-phase, suggesting the M-phase has higher symmetry. Surprisingly, when fifteen different elements with a total doping concentration of 3 $_{mol}$% are doped into Nb_2O_5 and then heated in air to 950 °C, the originally expected H-phase and other impurity phases do not appear. Instead, a singular phase resembling the M-phase like Nb_2O_5 emerges (Fig. 1c). Even at 1050 °C, this sample, termed HED-Nb_2O_5, maintains the M-phase like structure. This phenomenon, known as the high-entropy-doping effect, not only alters the phase transition pathway of Nb_2O_5 but also stabilizes a metastable structure.

To further investigate the high-entropy-doping effect, we selected twenty metallic elements (marked in red) from the periodic table in Fig. 1d for doping Nb_2O_5 with different numbers (horizontal axis) and concentrations (vertical axis, $_{mol}$%, molar ratio of doping metal ions to total metal ions) of elements. The doping concentration discussed here refers to the molar ratio of metal cations in the reaction container (i.e., the nominal composition). The doping composition utilizes an equimolar doping strategy, meaning all dopants are added in equal molar proportions. Due to the HED-Nb_2O_5's surprising stability and its inability to dissolve in aqua regia or hydrofluoric acid, we cannot determine the actual doping levels in the final samples by inductively coupled plasma (ICP) measurement. However, based on the time of flight secondary ion mass spectrometry (ToF-SIMS) analysis (Fig. S1), we can qualitatively assert that the elements have been successfully

https://doi.org/10.1038/s41467-025-60186-6

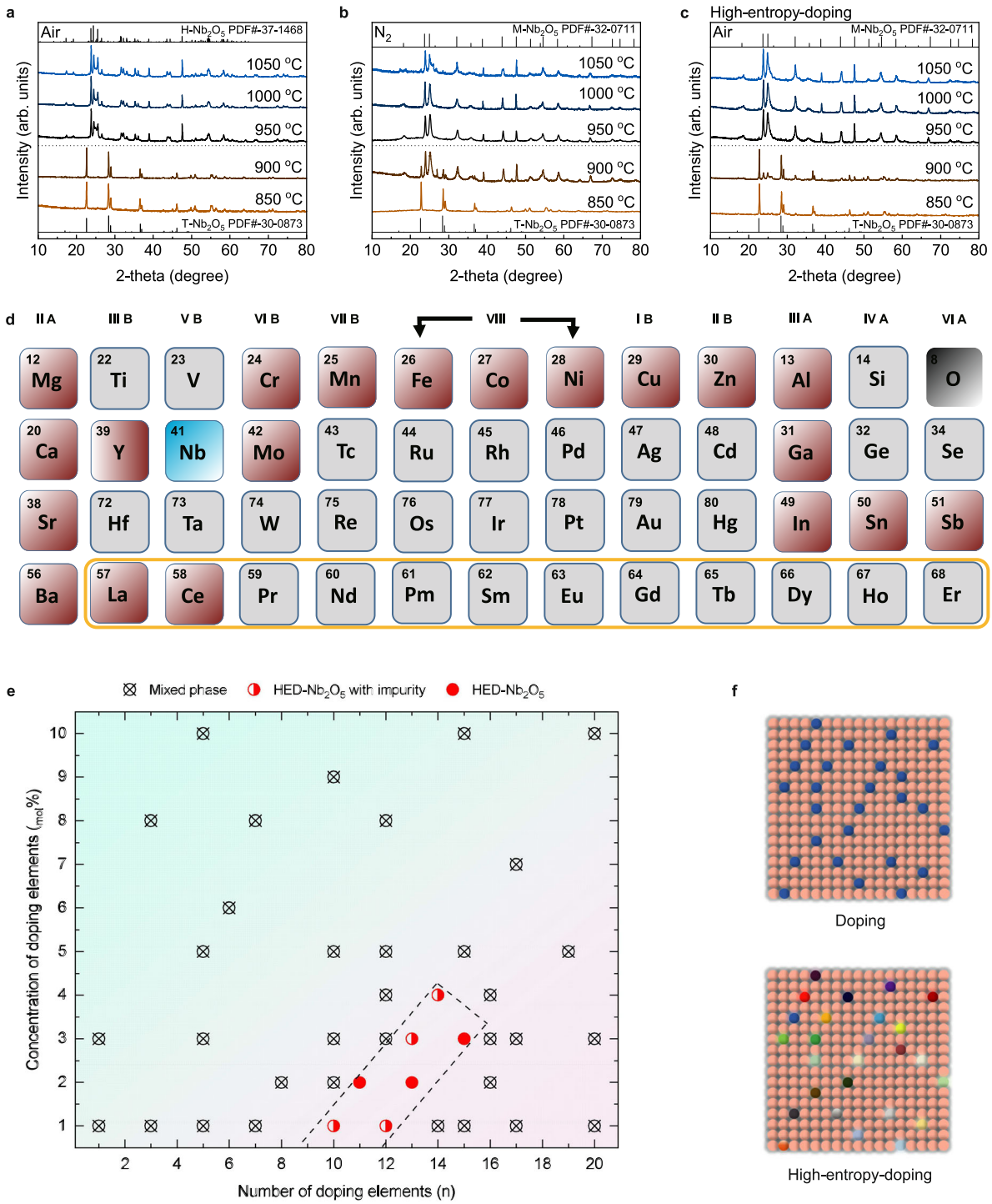

Fig. 1 | The high-entropy-doping effect in Nb_2O_5. **a**–**c** XRD patterns of Nb_2O_5 phases observed upon heating niobium oxalates in air (**a**) and nitrogen (**b**), and high-entropy-doped niobium oxalate in air (**c**) at different temperatures. The standard PDF patterns for T-(orthorhombic), M-(orthogonal), and H-(monoclinic) phase are inserted at the bottom and top of the graphs, respectively. **d** The periodic table of selected doping elements for Nb_2O_5. **e** The phase-state distribution of doped Nb_2O_5, including mixed phase, HED-Nb_2O_5 with impurity and HED-Nb_2O_5. The square broken line area refers to the high-entropy-doping region. **f** Schematic illustrations of conventional doping and high-entropy-doping.

incorporated into the sample's lattice. Regarding the selection of doping elements in Fig. 1d, we first excluded radioactive elements, precious metals, and expensive metallic elements. Secondly, we eliminated elements such as Li, which may undergo electrochemical insertion-extraction reactions. Moreover, we excluded elements like Ti and W, which are diagonally opposite to Nb in the periodic table and share similar chemical properties. On this basis, we selected these 20 elements as shown in Fig. 1d and prioritized doping with elements like Mg, Zn, and Ni, which are widely studied for their ability to induce phase transitions. We did not apply any further selection process for the elements when doping with a large variety of elements. We summarized the foundational characteristics of the selected doping ions in Table S1. Notably, both Mg and Zn have a valence state of 2+ and similar ionic potentials, both much lower than that of Nb^{5+}'s. This aligns

with prior reports that Mg^{2+} and Zn^{2+} promote the formation of two-dimensional niobates[13,15]. Similarly, Sr^{2+} and Ba^{2+}, with ionic radii larger than Nb^{5+}'s and lower ionic potentials, are prone to creating oxygen vacancies. In contrast, Mo^{6+} closely matches Nb^{5+} in terms of valence state, ionic radius, and ionic potential. Therefore, the selected elements encompass a wide range of doping conditions, offering comprehensive experimental validation for the high-entropy-doping effect.

After analyzing the XRD data from fifty doped Nb_2O_5 samples, we found that most of doped samples occur phase transition and form mixed phases after doping. However, in the inclined region shown in Fig. 1e, due to the specific range of doping element numbers and concentrations, an almost entirely pure HED-phase area emerged, known as the high-entropy-doping region. Specifically, the term "impurity" in Fig. 1e denotes the formation of other phases, such as two-dimensional phases or shear phases. We confirmed through repeated experiments that the observed feature in this region (Fig. 1e) is consistent and does not change with different dopant elements. The region demonstrates that the high-entropy-doping effect possess the intrinsic emergence induced by complex ions doping. Doped Nb_2O_5 within this area exhibit the exact phase transition pathway as shown in Fig. 1c, resulting in a HED-phase similar to the M-phase. The appearance of this high-entropy-doping region can be attributed to the inherent emergence of high-entropy-doping effect, as well as the system's configurational entropy reaching a maximum. However, the deeper mechanisms of this emergence remain a topic for further discussion.

In conventional doping methods, researchers typically explore which elements are suitable for doping, why these elements are chosen, and how they affect the electronic and crystal structures. However, when the number of doping elements increases, as shown in Fig. 1f, the concentration of any single dopant becomes very low, and the number of microscopic states in the system increases dramatically. While individual dopants may still exert their specific chemical effects, we believe that, in this case, more attention should be paid to the overall changes in the system. The difference between high-entropy-doping and conventional doping can be simply illustrated in schematic (Fig. 1f), showing the high-entropy-doping approach achieved by increasing the variety of doping elements.

Characteristic of high-entropy-doping effect

The fifty samples in Fig. 1d were named based on the numbers of doping elements (N) and the concentrations of doping elements (C) (detailed in Fig. S2 and Table S2). With further subdivision of doping conditions, three distinct influencing factors of high-entropy-doping could be identified as shown in Fig. 2. First is the impact of the number of doping elements on the Nb_2O_5 phase (Fig. 2a). With a fixed doping concentration of 3 $_{mol}$%, increasing the number of doping elements from 1 to 13 led to a gradual decrease in the amount of impurities including the typical two-dimensional phase and a refinement of the main peaks around 25 degree, resulting in very low levels of impurities in HED-Nb_2O_5-N13C3, which is also marked with a semi red circle in Fig. 1e. When the number of doping elements increased to 15, the impurities completely disappeared, marked with a full red circle. Interestingly, when the number of doping elements exceeds 15, the impurity phase sharply increases and HED-Nb_2O_5 decays, indicating there is a maximum threshold for the number of doping elements in high-entropy-doping effects. Secondly, the impact of doping concentration on Nb_2O_5 is examined. In Fig. 2b, the number of doping elements is kept at 15, and when the doping concentration is 1 $_{mol}$%, a secondary peak induced by shear phase could be observed around the main peak at about 25 degree. However, when the doping concentration reaches to 3 $_{mol}$%, the secondary peak disappears, and as the doping concentration further increase, more impurity phases are observed. This is different from the case when the number of doping elements is 12, where HED-Nb_2O_5 could only be obtained at a low concentration of 1 $_{mol}$%. The third aspect is the influence of substituting doping elements on Nb_2O_5 as shown in Fig. 2c. At a doping concentration of 5 $_{mol}$%, substituting all five doping elements always result in the formation of mixed phases, indicating that the type of elements is not the cause of impurity formation. In contrast, when we substituted doping elements in the HED-Nb_2O_5-N15C3 sample, we did not observe the formation of any impurity phases, further indicating that the high-entropy-doping effect is independent of the type of elements but related to the number of element types, demonstrating the inherent rigidity of the high-entropy-doping effect.

Spectroscopic properties and microscopic morphology of HED-Nb_2O_5

Using scanning electron microscopic (SEM) energy-dispersive spectra (EDS) mapping analysis, we further confirmed the uniform dispersion of doping metal elements within the HED-Nb_2O_5 particles, as shown in Fig. 2d. In contrast, as shown in Fig. S3, the EDS mapping of Nb_2O_5-N12C5 shows that Sr^{2+}, Mo^{6+}, and Ca^{2+} elements may exhibit non-uniform distributions, while in Nb_2O_5-N20C3, Mg^{2+} and Sb^{3+} also appear to be unevenly distributed. These findings, supported by EDS mapping, further validate the success of high-entropy-doping.

To fully understand the functions of high-entropy-doping on Nb_2O_5, we investigated the physicochemical properties of HED-Nb_2O_5-N15C3 (hereafter referred to as HED-Nb_2O_5) and also prepared the other four most commonly niobium oxide phases for comparison. From the XRD patterns in Fig. S4, it is obviously that TT-Nb_2O_5 and T-Nb_2O_5 structures are similar, as T-Nb_2O_5 is regarded as the fully crystallized TT-Nb_2O_5. While HED-Nb_2O_5 had a crystal structure close to that of M-Nb_2O_5 and H-Nb_2O_5. From the Rietveld refinement as shown in Fig. 3a, M-, HED-, and H-Nb_2O_5 all belong to Wadsley-Roth family. H-Nb_2O_5 exhibits a crystallographic shear structures at the borders of $(3\times4)_1$ and $(3\times5)_\infty$ ReO_3-like blocks of NbO_6 octahedra with a space group of *P2/m*, while M- and HED-Nb_2O_5 possess $(3\times4)_\infty$ ReO_3-like blocks with a space group of *Cmcm* (the subscripts 1 and ∞ represent the connectivity of blocks in the *ac* plane)[9,25–28]. The blocks are infinitely connected, offering open tunnel-like Li^+ diffusion channels throughout crystals. The Rietveld refinement data obtained using laboratory XRD equipment. This provides crucial evidence for the formation of the target phase, the limitations of the laboratory setup mean that dopant atom occupancy cannot be directly determined. To further understand the structural impact of doping, we incorporated additional techniques, including Raman spectroscopy, X-ray photoelectron spectroscopy (XPS), transmission electron microscopy (TEM), and electron paramagnetic resonance (EPR), which collectively aid in elucidating the dopant-induced changes in the crystal structure and related properties.

The Raman spectra in Fig. 3b displayed astonishingly similar trends to the XRD patterns. The broader Raman band for TT- and T-Nb_2O_5 is due to the NbO_6 and NbO_7 niobium coordinations. As the phase changes from TT- and T-Nb_2O_5 to M-, HED-, and H-Nb_2O_5, a gradual increase in the bending mode of Nb-O-Nb at 200–300 cm^{-1}, the stretching mode of NbO_x at 600–750 cm^{-1} and the stretching mode of a higher-order bond (Nb = O terminal bond) with a shorter bond distance was noted, indicating strengthened Nb = O bonds and intensified Nb-O-Nb interactions[25,29]. The Raman features suggested that the local bonding modes of HED-Nb_2O_5 are between those of the M- and H-phases but not exactly identical to either. The Nb and O exhibits rich spectral states in XPS as shown in Fig. 3c. The TT-Nb_2O_5 shows a typical Nb^{5+} valence state, while the T-Nb_2O_5 exhibits a state closer to that of the M-Nb_2O_5. This suggests that obtaining the T-phase is likely accompanied by a large number of oxygen vacancies. However, unlike the M-Nb_2O_5 and HED-Nb_2O_5 show similar crystal structures from XRD patterns, the chemical states of Nb and O in HED-Nb_2O_5 is evidently closer to H-Nb_2O_5 rather than M-Nb_2O_5. Combined with Raman

https://doi.org/10.1038/s41467-025-60186-6

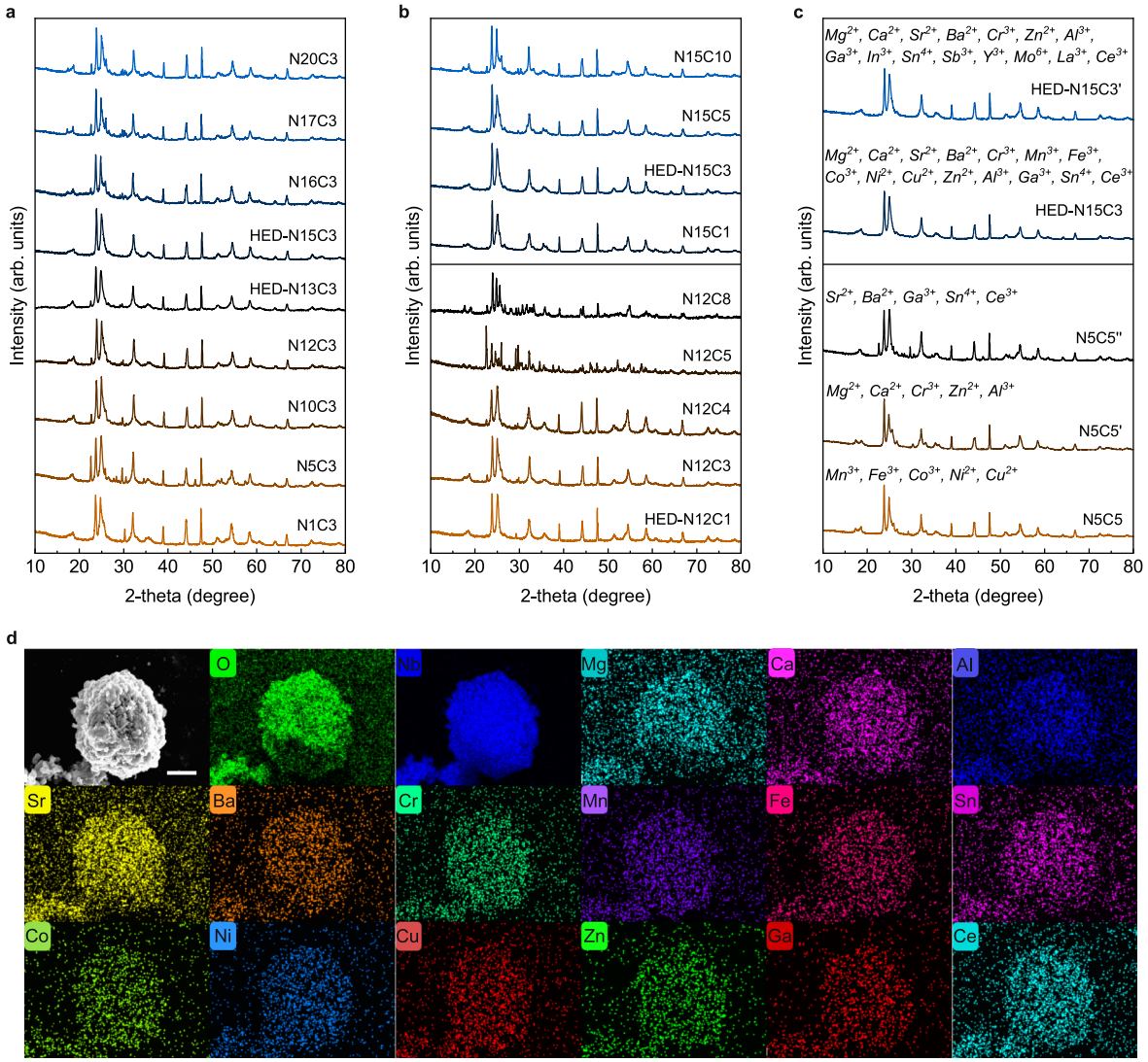

Fig. 2 | The phase evolution of doped Nb_2O_5 influenced by number, concentration, and substitution of doping elements and the microscopic morphology of HED-Nb_2O_5. **a** XRD patterns of Nb_2O_5-C3 with the different numbers of doping elements at a doping concentration of 3%. **b** XRD patterns of Nb_2O_5-N12 and Nb_2O_5-N15 with the different doping concentrations. **c** XRD patterns of Nb_2O_5-N15C3 and Nb_2O_5-N5C5 with the substitution of doping elements with their corresponding possible oxidation states. The specific dopants of Nb_2O_5-NXCY can be found in Table S2. **d** The SEM-EDS mappings of HED-Nb_2O_5 (N15C3, doping elements: Mg, Ca, Al, Sr, Ba, Cr, Mn, Fe, Sn, Co, Ni, Cu, Zn, Ga, Ce). Scale bar, 2 μm.

spectroscopy, this implies that HED-Nb_2O_5 represents a completely new material state[30]. The analysis based on EPR further studies the types of oxygen vacancies for niobium oxides through the paramagnetism of unpaired electrons. The results from Fig. S5 illustrate that high-entropy-doping has a complex impact on the oxygen vacancies in niobium oxide. In the EPR signals from the H- and M-phases, the signal strengths related to oxygen vacancies are comparable, but the H-phase likely has a slightly higher density of oxygen vacancies. In the EPR signals from HED-Nb_2O_5, we observe a pronounced splitting behavior of the oxygen vacancy signals, with high peak intensities, indicating that high-entropy-doping substantially complicates the structure of oxygen vacancies in niobium oxide[31]. Upon analyzing the EPR signals of H-Nb_2O_5 and M-Nb_2O_5, we find that the types of oxygen vacancies are consistent, with a slightly higher concentration of oxygen vacancies in the H-phase compared to the M-phase. However, in the HED-Nb_2O_5 sample, at least five different types of oxygen vacancies are observed[32–34], with an overall oxygen vacancy concentration higher than in both the M-phase and H-phase. Moreover, the doping of transition metal ions and rare-earth metal ions leads to a strong spin-orbit coupling effect, which gives rise to a g-factor of 4.06[35,36]. The phenomenon directly reflects that high-entropy-doping enhances the complexity of the niobium oxide lattice structure.

Although these five niobium oxide phases are all prepared from the same precursor, their SEM images (see Fig. S6) show significant differences. Interestingly, these differences are consistent with the results of spectral results. The TT- and T-Nb_2O_5 have similar morphologies, both consisting of nanoparticles with sizes ranging from tens to hundreds of nanometers. However, after increasing the annealing temperature, the particle sizes of the M- and H-Nb_2O_5 are around several micrometers, indicating that not only phase transitions occurred around 900 °C, but also the particles molten and merged into larger-sized particles[37]. Notably, the high-entropy-doping effect makes the HED-Nb_2O_5 particles appear more rounded. We conducted a

https://doi.org/10.1038/s41467-025-60186-6

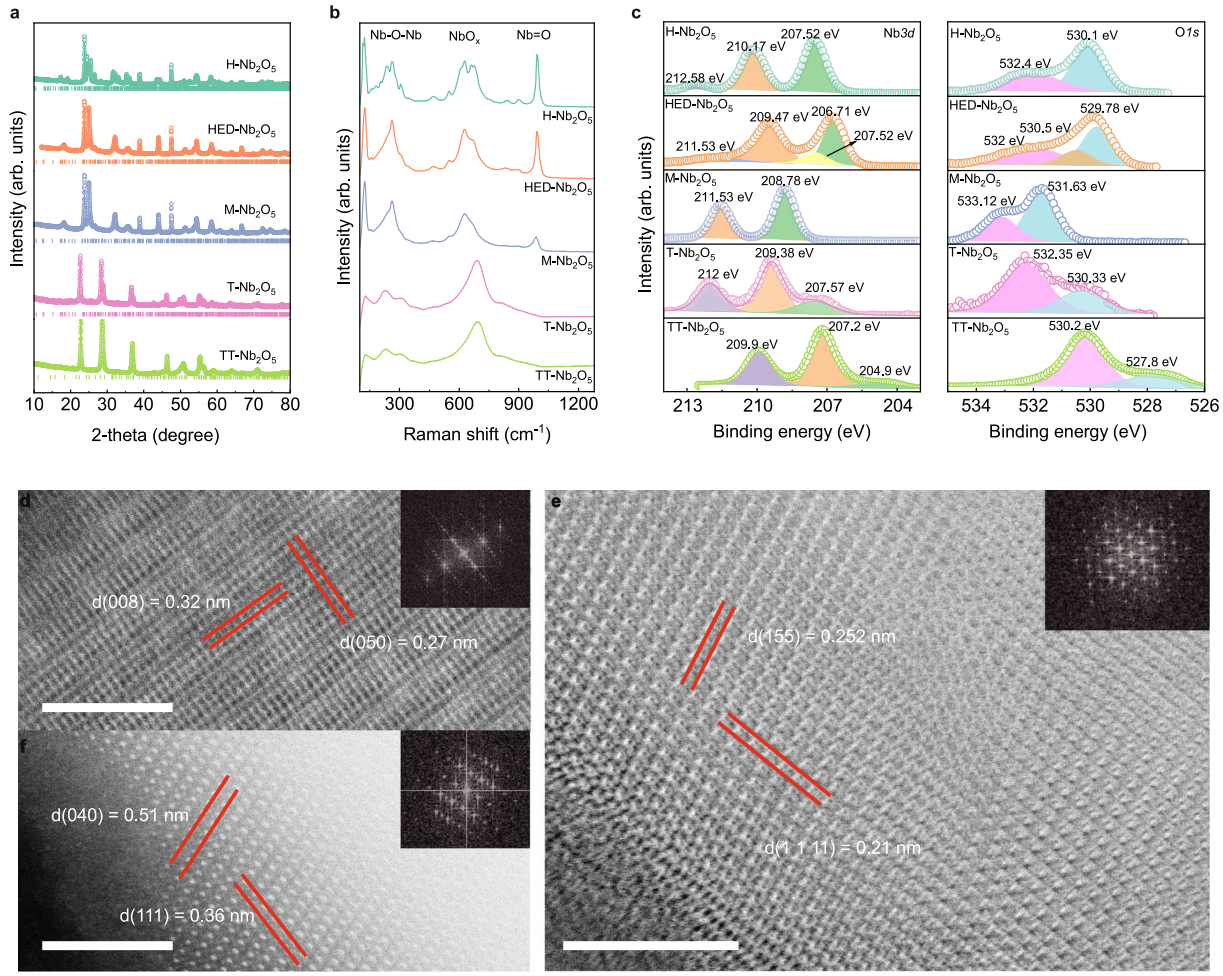

Fig. 3 | The spectral and structural characterizations of HED-Nb_2O_5. **a** Rietveld refinements of powder XRD patterns, **b** Raman spectra and **c** XPS spectra of TT-, T-, M-, HED-, and H-Nb_2O_5. **d**–**f** TEM images, and corresponding FFT (fast Fourier transform) patterns of HED-Nb_2O_5. Scale bar, 5 nm. The colour gradient from Tibetan green to grass green in (**a**–**c**) represents from H-Nb_2O_5 to TT-Nb_2O_5, respectively.

more detailed TEM observation of HED-Nb_2O_5 from various crystallographic directions. The results demonstrate that the material has a high degree of crystallinity and no grain boundaries were observed. Particularly in Fig. 3e, besides the clearly visible (155) and (1 1 11) crystal planes, the lattice fringes also exhibited some variations, primarily due to the selected observation direction being extremely sensitive to the electron beam projection angle, where even minor defects causing slight internal angular changes in the particles can lead to significant fluctuations in the lattice fringes.

The battery performances and electrochemical behavior of HED-Nb_2O_5

As a fast-charging negative electrode material for Li-ion battery, we investigated the battery performance and electrochemical behavior of HED-Nb_2O_5 compared with the other four undoped phases. The galvanostatic charge-discharge curves (Fig. 4a) reveal that HED-Nb_2O_5 maintains the rapid-charging capabilities characteristic of Nb_2O_5, demonstrating significant capacity output over a wide range of charge-discharge rates from 0.1 A g^{-1} to 40 A g^{-1} within a voltage window of 1–3 V vs. Li^+/Li. At 1 A g^{-1}, the charging capacity reaches 233.9 mAh g^{-1}, and at a specific current of 40 A g^{-1}, the capacity still achieves 88.9 mAh g^{-1}. Additionally, the charge-discharge capacity remains stable within a single voltage plateau up to 10 C, as shown in the derivative plot (Figs. 4b, S7, and S8). By comparing the electrochemical properties of HED-Nb_2O_5 with four other typical undoped crystal phases of Nb_2O_5 (TT-, T-, M-, H-Nb_2O_5) within the 1–3 V vs. Li^+/Li electrochemical window (Fig. 4c), HED-Nb_2O_5 exhibits overwhelming rate performance over the others, especially at rates from 10 A g^{-1} to 40 A g^{-1}, where it maintains high capacity far exceeding that of the other phases. As shown in Fig. S9a, further validation showed that the high-rate performance exhibits some variation at 40 A g^{-1}, with capacities estimated between 60 and 80 mAh g^{-1}, likely influenced by temperature fluctuations. To study the electrochemical performances of other doped Nb_2O_5 with impurities, we selected 5 typically doped samples to conduct electrochemical testing (Fig. S9). We found that HED-Nb_2O_5 retains its unparalleled rate advantage at high rates (150 C and 200 C). However, under lower rate conditions (less than 20 A g^{-1}), some doped samples containing impurity phases exhibited higher capacity than HED-Nb_2O_5 as shown in Fig. S9. This is clearly due to impurity induced by doping, which can contribute additional capacity. We further characterized and compared the rate performance of H-Nb_2O_5 and HED-Nb_2O_5 at higher areal mass loadings to demonstrate the practical significance of high-entropy-doping effect. When the areal mass loading was increased to a high level (Fig. S10a, b), it was observed that HED-Nb_2O_5 still exhibited a much higher capacity than H-Nb_2O_5 at high rates. For instance, at a loading of 6 mg cm^{-2} and a rate of 2 A g^{-1}, the high-entropy-doped sample achieved a

https://doi.org/10.1038/s41467-025-60186-6

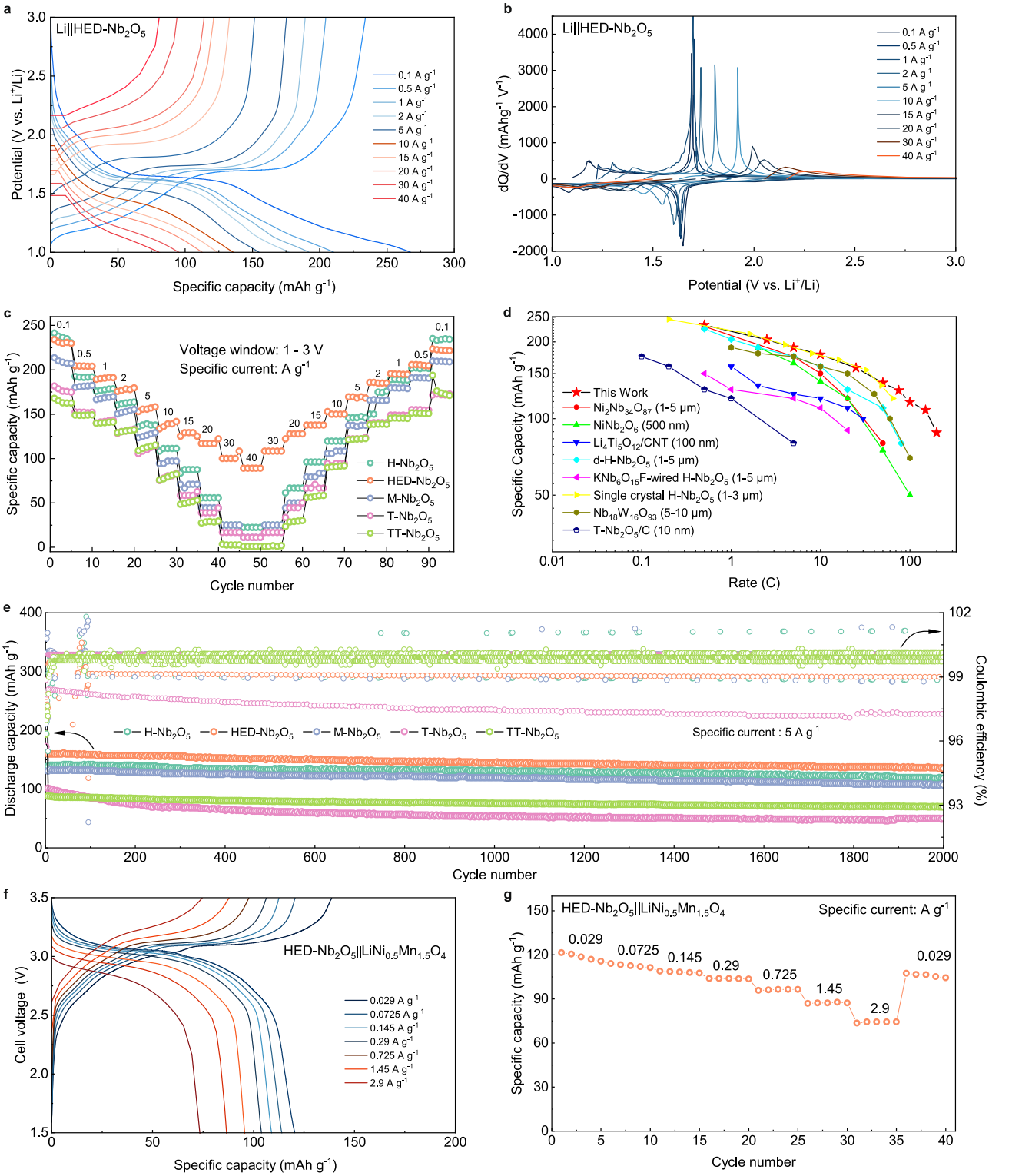

Fig. 4 | The battery performances of HED-Nb_2O_5. **a**, **b** Galvanostatic discharge and charge curves (**a**) and dQ/dV plots (**b**) (Q, capacity; V, voltage) of HED-Nb_2O_5. **c** Rate performance summary of niobium oxides. **d** Rate performance comparison of HED-Nb_2O_5 and other reported high-rate negative electrode materials. **e** High-rate cycling performances of niobium oxides for 2000 cycles at 5 A g^{-1}. **f**, **g** Galvanostatic discharge and charge curves (**f**) and rate performances (**g**) of HED-Nb_2O_5||$LiNi_{0.5}Mn_{1.5}O_4$ full cell. The calculation of specific current and specific capacity (**f**, **g**) is based on mass loading of $LiNi_{0.5}Mn_{1.5}O_4$.

capacity close to 130 mAh g^{-1}, while the undoped H-Nb_2O_5 showed only about 60 mAh g^{-1}.

Comparisons with several typical fast-charging negative electrode materials (including Nb_2O_5 derivative $Nb_{18}W_{16}O_{93}$, nano-Nb_2O_5 encapsulated with carbon particles and the classic fast-charging negative electrode material $Li_4Ti_5O_{14}$)[9,14,25,38–42] using identical cell architectures and comparable electrode/electrolyte parameters, HED-Nb_2O_5 shows rate advantages at rates greater than 10 A g^{-1}, confirming it as a fast-charging negative electrode material (Fig. 4d). Table S3 systematically compares key parameters including active material

loading, conductive carbon content, membrane type, electrolyte composition, and high-rate performance with specific capacity at corresponding current densities. Niobium oxides generally deliver good electrochemical cycling stability in HED-Nb_2O_5, as shown in Fig. 4e. Specially, when cycled at a high specific current of 5 A g^{-1}, HED-Nb_2O_5 maintains 85% of its initial capacity over 2000 cycles with Coulombic efficiency consistently approaching 100%. The full-cell performance based HED-Nb_2O_5 negative electrode is also investigated as shown in Figs. 4f and 4g. Paired with the high-voltage positive electrode $LiNi_{0.5}Mn_{1.5}O_4$, it maintains a cathodic capacity of 120 mAh g^{-1} at 0.0725 A g^{-1} and 75 mAg^{-1} at 2.9 A g^{-1}, which is superior to a lithium manganese nickel oxide full-cell using $TiNb_2O_7$ as an negative electrode[43]. The assembled full-cell achieves a specific energy of 221.3 Wh kg^{-1} at 0.029 A g^{-1}, with a specific power of 51.9 kW kg^{-1}, and at a specific current of 2.9 A g^{-1}, the specific power increases to 896 kW kg^{-1}, reaching an specific energy of 44.8 Wh kg^{-1} (based on the total mass of positive electrode and negative electrode). Notably, as the specific current increases as shown in Figs. 4f and S10c, Coulombic efficiency exhibits a marked improvement, approaching near-ideal values (~100%). In contrast, lower specific current results in comparatively inferior Coulombic efficiency performance (86.8% at 0.029 A g^{-1}). This suggests that the baseline electrolyte fails to effectively suppress parasitic side reactions under high-voltage operation. The mitigation of such side reactions at elevated specific currents may be attributed to the reduced cumulative impact of electrochemical degradation processes during shorter charge/discharge durations. These underscore the critical need for further electrolyte engineering efforts, specifically targeting enhanced electrode-electrolyte compatibility and kinetic stabilization.

Regarding the specific chemical effects of the doping elements, we speculate that alkaline earth metals like Mg, Ca, Sr, and Ba mainly enhance performance by introducing oxygen vacancies; 3 d transition metals like Cr, Mn, Fe, Co, Ni, Cu, and Zn not only introduce oxygen vacancies but also improve conductivity through interactions between their 3 d electrons and Nb's 4 d electrons; Al helps stabilize the lattice structure; Ga, In, Sn, and Sb may enrich the Nb's 4 d electronic structure; and rare earth elements like Y, La, and Ce likely help reduce porosity of particle and improve density of material. Our research on the battery performance clearly demonstrates the enhancement of high-entropy-doping effect on the battery performance of Nb_2O_5.

We have also meticulously investigated the electrochemical properties of HED-Nb_2O_5 by galvanostatic intermittent titration technique (GITT, Fig. S11). The linearity of potential-concentration validate diffusion coefficient calculations. Figure 5a displays the diffusion coefficients of all five Nb_2O_5 materials. Despite the smaller particle size of TT- and T-phases, better diffusion coefficients are observed across the entire charge-discharge region for H-, HED-, and M-phases, with HED-Nb_2O_5 showing higher diffusion coefficient at the voltage plateau region compared to M- and H-phases. This corresponds to the rate performances and voltammetric behaviors of niobium oxide phases. Since TT-Nb_2O_5 has the lowest diffusion rate, it also shows the poorest rate performance. HED-Nb_2O_5 exhibits the highest diffusion coefficient at the voltage plateau around 1.7 V vs. Li^+/Li, hence the best rate performance. It is important to note that during the electrochemical intercalation reaction around 1.7 V vs. Li^+/Li, the diffusion coefficient reaches its minimum, which has a significant impact on rate performance. We observe that the minimum diffusion coefficient for the HED-Nb_2O_5 (4.2×10^{-10} m^2s^{-1}) is higher than that of the M-Nb_2O_5 (7.1×10^{-10} m^2s^{-1}), which in turn is higher than that of the H-Nb_2O_5 (9.5×10^{-11} m^2s^{-1}). This observation aligns with the trend in rate performances. In addition to the high-entropy-doping effect, it is also essential to consider the particle size differences shown in Fig. S6. H-Nb_2O_5 particles are the largest and roughest, with significant aggregation and sizes ranging from 3 to 6 μm; M-Nb_2O_5 particles are generally 2 ~ 3 μm; and HED-Nb_2O_5 particles are the smallest, 1 ~ 2 μm, and more uniform. These results suggest that the reduction in particle size shortens the diffusion pathway, which may be another critical factor contributing to the rate performance of the HED phase.

Through cyclic voltammogram (CV) curves (Fig. 5b), TT-Nb_2O_5 and T-Nb_2O_5 share similar CV profiles, as do M-Nb_2O_5, H-Nb_2O_5, and HED-Nb_2O_5. Augustyn et al. analyzed niobium oxide's high-rate performance based on the relationship $i = av^b$, where i refers to the current and v is the sweep rate (mV s^{-1}) of cyclic voltammetry experiment[10]. It is concluded that a b-value close to 1 is due to pseudocapacitance. Similarly, the redox peak positions of these five oxides have been fitted, and Fig. S12 shows that the b-values for TT-Nb_2O_5 and T-Nb_2O_5 are closer to 1, indicating a surface-controlled process, also known as the embedded pseudocapacitive effect. Conversely, M-Nb_2O_5, H-Nb_2O_5, and HED-Nb_2O_5 all exhibit a significant pair of reversible redox peaks at 1.65/1.69 V vs. Li^+/Li, with respective b-values of 0.845, 0.735, 0.728, indicating processes controlled by both diffusion and surface effects. It is noteworthy that even both with a b-value of 1, T-Nb_2O_5 still shows superior rate performance compared to TT-Nb_2O_5. Additionally, niobium oxide can still exhibit high-rate performance with a b-value less than 1, demonstrating that the so-called intercalated pseudocapacitance does not fully explain the root of Nb_2O_5's fast-charging capabilities, and also the existence of intercalated pseudocapacitance should remain controversial. Operando XRD testing and analysis (Fig. 5c, d) reveal that during the entire charge-discharge process, all three Nb_2O_5 phases undergo a two-phase transition, with similar and small changes in unit cell volume. Moreover, all three phases undergo a phase transition after the insertion of approximately 0.5 lithium ions, and the lattice exhibits significant expansion upon further lithium ion insertion. This suggests that for the Wadsley-Roth structured Nb_2O_5 formed at high temperatures, their phase evolution from operando XRD patterns are completely similar under low rates or quasi-equilibrium conditions. These are consistent with findings of previous reports[9,19,32], which also identify niobium oxides as one of the key materials for fast-charging. Although the phase evolution of these niobium oxides during charge and discharge are clearly shown in Fig. 5c–e, we still cannot identify the exact reason for the rate performance improvement with high-entropy-doping from the phase evolution at the low rate conditions. Due to the intensity limitation of lab X-ray source, we are currently unable to obtain phase evolution data under high rates, and operando synchrotron X-ray experiments are needed to investigate this aspect in the future.

Discussion

Doping, as the most widely applied modification technique in the field of materials research, has been systematically studied. However, such traditional studies have always focused on the working mechanisms by which one or several elements affect the crystal or electronic structures of materials. High-entropy-doping, markedly different from the traditional doping approaches, does not confine itself to exploring the specific effects of one or a few elements on the materials. Instead, it places the variety and quantity of doping elements at the core of its research, aiming to introduce new physical or chemical phenomena by increasing the system's complexity or "more is different". The significance of high-entropy-doping lies in its potential to achieve these effects by altering the symmetry of the material system.

It is important to note that high-entropy-doping, which seeks to modify the inherent properties of a specific material through the entropy of doping elements, is not synonymous with high-entropy materials. From the perspective of configurational entropy, the extensively studied high-entropy materials should represent merely an idealized manifestation within highly miscible multi-element systems, whereas the more universal paradigm emerging from high-entropy related materials is fundamentally rooted in high-entropy-doping effect.

https://doi.org/10.1038/s41467-025-60186-6

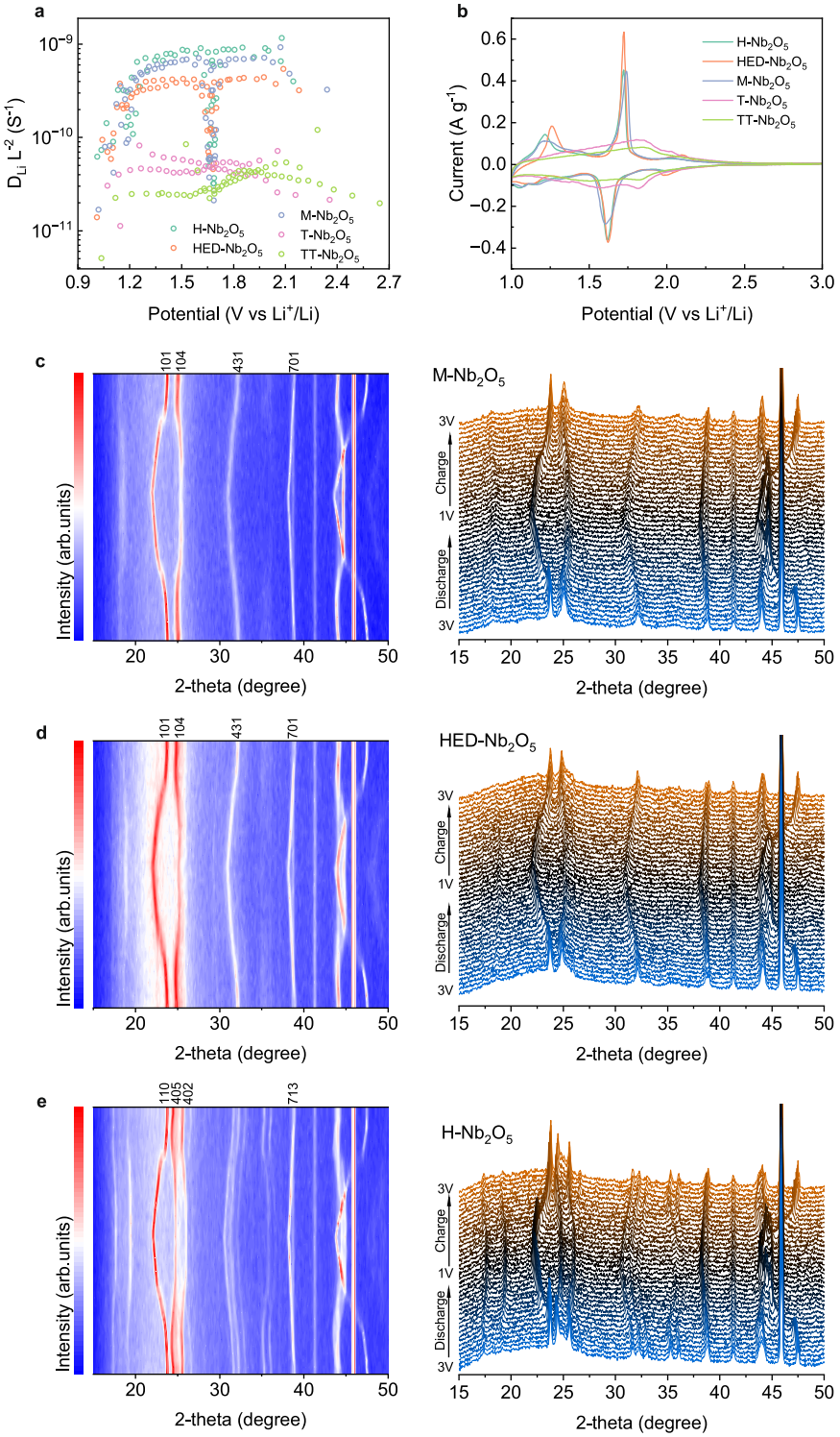

Fig. 5 | The electrochemical properties of HED-Nb_2O_5. a Lithium diffusion coefficients of TT-, T-, M-, HED-, and H-Nb_2O_5 as a function of open-circuit voltage, calculated from galvanostatic intermittent titration technique (GITT) curves. **b** Cyclic voltammogram (CV) of the niobium oxides at a sweep rate of 0.1 mV s^{-1}. **c**–**e** The operando XRD patterns of (**c**) M-, (**d**) HED-, and (**e**) H-Nb_2O_5 at a specific current of 25 mA g^{-1} and a temperature of 27 °C.

High-entropy-doping effects should be explained using phase transition theory. Since the annealing temperature T and pressure P remain unchanged in our samples of Fig. 1e, we can modify the thermodynamic potential from the well-known $\Phi(P, T, \eta)$ to $\Phi(N, C, \eta)$, where N is the number of doping element species, C is the doping concentration, and η is the order parameter defined according to the overall symmetry of the resulting phases. We hypothesize that when high-entropy-doping effects occur and N and C reach critical values, the function $\Phi(N, C, \eta)$ may exhibit a minimum. A more rigorous mathematical proof needs to be provided by theorist in phase transition field.

In our research, we reported an emergent and rigid high-entropy-doping effect in the lithium-ion rapid-charging negative electrode material Nb_2O_5. This effect not only achieved effective doping of Nb_2O_5 but also substantially enhanced its electrochemical properties. We believe our study and elucidation of the high-entropy-doping

effect hold the promise of contributing new phenomena in fields of material research such as energy materials, semiconductors, luminescent materials, topological materials, etc[44–46].

Methods

Doping solutions preparation

The doping solutions were prepared by dissolving the following corresponding reagents in an amount of 50 ml deionized water: $MnC_4H_6O_4{\cdot}4H_2O$ (Aladdin, 99%, 39.2 mg), $Fe(C_2H_3O_2)_2$ (Aladdin, 99%, 27.8 mg), $C_4H_6CoO_4{\cdot}4H_2O$ (Aladdin, 99.5%, 39.8 mg), $NiC_4H_6O_4{\cdot}4H_2O$ (Aladdin, 99%, 39.8 mg), $CuC_4H_6O_4{\cdot}H_2O$ (Macklin, 99%, 31.9 mg), $ZnC_4H_6O_4$ (Aladdin, 99%, 29.3 mg), $MgC_4H_6O_4{\cdot}4H_2O$ (Aladdin, 99%, 34.3 mg), $CaC_4H_6O_4$ (Macklin, 99%, 25.3 mg), $Al(NO_3)_3{\cdot}9H_2O$ (Innochem, 99%, 60 mg), $SnCl_4{\cdot}5H_2O$ (Macklin, 99%, 56 mg), $Ga(NO_3)_3{\cdot}H_2O$ (Macklin, 99%, 40.9 mg), $SrCl_2{\cdot}6H_2O$ (Aladdin, 99%, 42.7 mg), $BaCl_2{\cdot}H_2O$ (Aladdin, 99%, 39 mg), $CeCl_3{\cdot}7H_2O$ (Aladdin, 99%, 59.6 mg), $CrC_6H_9O_6$ (Aladdin, 99.9%, 36.7 mg), $H_{24}Mo_7N_6O_{24}{\cdot}4H_2O$ (Aladdin, 98%, 197.7 mg), $C_6H_9O_6Sb$ (Aladdin, 99%, 47.8 mg), $In(C_2H_3O_2)_3$ (macklin, 99%, 46.7 mg), $H_2N_3O_{10}Y$ (macklin, 99%, 46.8 mg), and $LaN_3O_9{\cdot}6H_2O$ (Macklin, 99%, 69.2 mg). The solution is magnetically stirred until clear and clarified, then stored at a low temperature. All dopant elements are incorporated in an equimolar ratio.

Materials synthesis

Niobium oxalate (Macklin, $NbC_{10}H_5O_{20}$, 99%, weight: 4.175 g) was dissolved in 100 ml deionized water and stirred magnetically for 30 min. In order to precisely control the doping amount, the calculated mass of the prepared doping solutions was weighed and added to the niobium oxalate solution, followed by 30 min of magnetic stirring. The mixture was then heated and stirred at 60 °C until complete evaporation of the deionized water. The resulting precursor was subjected to pre-firing at 500 °C for 3 h with a ramp rate of 5 °C min^{-1}. Subsequently, the sample was ground for 10 min using a mortar and then annealed at 1000 °C for 2 h with a ramp rate of 5 °C min^{-1} to obtain the doped Nb_2O_5. For preparation of H-Nb_2O_5, T-Nb_2O_5, and TT-Nb_2O_5, the niobium oxalate was grounded with a few amount of ethanol and then annealed at 1000 °C, 700 °C, and 500 °C for 3 h with a ramp rate of 5° C min^{-1} at air atmosphere, respectively. For preparation of M-Nb_2O_5, the niobium oxalate was also grounded with a few amount of ethanol and then annealed at 1000 °C for 3 h with a ramp rate of 5 °C min^{-1} at nitrogen atmosphere. After the holding period, all samples were naturally cooled to room temperature within the muffle furnace or tube furnace.

Electrochemical measurements

A slurry is manually prepared using the classical electrode sheet preparation method by grinding the active material Nb_2O_5, superconducting carbon black (KLD Co., Ltd.), and polyvinylidene difluoride (HVSV900, molar weight 1000 kDa) in an 8:1:1 ratio in a mortar, with N-methyl-2-pyrrolidone (NMP, Aladdin, 99%) as the solvent. For electrode slurry preparation, the solvent (NMP) to solid (include active material, conductive additive, binder) ratio was maintained at around ~70:30 by weight. The slurry was mixed thoroughly to ensure homogeneity by manually grinding. The resulting slurry is single-side casting onto a copper foil, with careful control of the active substance load (1 ~ 1.2 mg cm^{-1}) using a doctor blade. The copper foil (thickness, 40 μm; purity > 99.5%) is preheated at 50 °C for 30 min, followed by overnight placement in a vacuum oven at 60 °C. Electrode sheets with a diameter of 12 mm are cut from the dried copper foil by a manual precision cutter (MTI, MSK-T10). The non-aqueous electrolyte, composed of 1 M lithium hexafluorophosphate ($LiPF_6$) in a solution of ethylene carbonate (EC): dimethyl carbonate (DMC): diethyl carbonate (DEC) (1:1:1 by volume, DoDochem, LB-014-100), is used alongside one disc of glass fiber membrane (Whatman GF/D; diameter, 16 mm; thickness, 675 μm; porosity, 80% ± 2%; 2.7 μm average pore diameter) and lithium metal (KLD-110, 15.6 mm × 0.45 mm (diameter × thickness), high purity of 99.9%) counter electrode for encapsulation within an argon-filled glove box. The non-aqueous electrolyte, glass fiber membrane, and lithium foil were used as received without further treatment. During assembly, a spring disc and a 1-mm-thick spacer were included. The amount of electrolyte used is controlled at 120 μl per cell. The half-cell (CR2032 coin type battery) is allowed to stand for 8 h before testing. Half cells were performed within 1.0–3.0 V vs. Li^+/Li. $LiNi_{0.5}Mn_{1.5}O_4$ is used as the positive electrode material for full-cell (CR2032 coin type battery), and its slurry and electrode sheet preparation process are the same as that of Nb_2O_5, except that aluminum foil is used as the current collector. The mass loading of $LiNi_{0.5}Mn_{1.5}O_4$ (KLD Co., Ltd., MA-EN-CA) is 2 ~ 2.5 mg cm^{-1}. The positive to negative mass ratio was controlled at 1.90 ± 0.05. The HED-Nb_2O_5 negative electrode and $LiNi_{0.5}Mn_{1.5}O_4$ positive electrode were sandwiched with a glass fiber separator and lithium metal foil an Ar-filled glovebox (<0.1 ppm O_2/H_2O). 120 μL of electrolyte (1 M $LiPF_6$ in EC:DMC:DEC 1:1:1 v/v/v) was injected to fully impregnate the $LiNi_{0.5}Mn_{1.5}O_4$/separator/Li metal stack. The assembled stack was allowed to rest for 12 h at 25 °C to ensure complete solid electrolyte interface pre-formation. The HED-Nb_2O_5 negative electrode was then paired with pre-activated $LiNi_{0.5}Mn_{1.5}O_4$ positive electrode material in full-cell assembled with a spring disc and a 1-mm-thick spacer. The specific energy and specific power of full cells were calculated based on: Specific Energy (Wh/kg) = Discharge Capacity (mAh/g) × Average Voltage (V)/1000; Specific Power (W/kg) = Specific Energy (Wh/kg)/Δt. Electrochemical measurements were conducted at a constant temperature of 27 °C using the 8-channel Neware battery testing system (CT 4008 T) in a voltage range of 1.5–3.5 V. The GITT experiments were conducted at a specific current of 0.1 C, a current pulse width of 0.5 h, and a rest period of 12 h to reach a quasi-equilibrium potential. The diffusion coefficients D_{Li} was extracted using the following equation to eliminate the effect of the electrode's circuitry[47,48]:

$$D_{Li} = \frac{4}{\pi\tau} L^2 \left(\frac{\Delta E_s}{\Delta E_t}\right)^2 \quad (1)$$

where τ is the duration of the current pulse, L is the diffusion length, ΔE_S is the change in steady-state potential, and ΔE_t is the total change in cell voltage during the current pulse after removing the ohmic loss. All electrochemical tests were conducted in an air-conditioned laboratory with temperature stabilized at 27.0 ± 1.0 °C.

Theoretical capacity of Nb_2O_5 is calculated by Faraday's equation: $Q_{theoretical} = nF/3.6\,m = 200$ mAh g^{-1}, where n (here $n = 1$) is the number of electrons transferred per formula unit, F is Faraday's constant, 3.6 is a conversion factor between coulombs and the conventional milliampere-hour (mAh) and m is the mass (g) per formula unit of Nb_2O_5. The C-rate is defined relative to one-electron transfer per transition metal, thus for Nb_2O_5, 1 C = 200 mA g^{-1}. The $Q_{theoretical}$ of $LiNi_{0.5}Mn_{1.5}O_4$ is set to 145 mAh g^{-1} in this work. The Coulombic efficiency (CE) = Discharge capacity (mAh g^{-1}) / Charge capacity (mAh g^{-1}).

The differential capacity (dQ/dV) was computed from galvanostatic data using OriginPro 2024 (OriginLab, USA). Potential (V vs. Li^+/Li) and capacity (Q) data were smoothed with 5-point adjacent averaging to minimize high-frequency noise. The derivative dQ/dV was calculated via a central difference algorithm and plotted against V to identify electrochemical characteristics.

Material characterization

Powder samples were grinded to fine particles using a mortar and pestle and then mounted onto a glass holder. A glass slide was used to smooth the surface for uniform scattering. XRD patterns was collected using the Rigaku Smart Lab diffractometer with Cu Kα radiation. Measurements were performed over a 2θ range of 10°–80° with a step size of 0.02° and a scan rate of 10° min^{-1} for standard samples, while high-resolution scans for Rietveld refinement employed a reduced

scan rate of 5° min^{-1} to enhance signal-to-noise ratios. Electrochemical operando XRD (BRUKER D8 Advance) measurements are conducted in the 2θ range of 15°–50° with a step size of 0.02° at a scan rate of 3.5° min^{-1}. It contains a hard, conductive glassy carbon window to prevent inhomogeneous electrochemical reactions, which are a concern with flexible or non-conductive X-ray windows. Owing to the absorbing nature of niobium and the absence of a current collector, self-standing electrodes were made with a 7:2:1 mass ratio of metal oxide: superconducting carbon black: poly(tetrafluoroethylene). All components were mixed thoroughly in a mortar using droplets of isopropanol as solvent, and then rolled into a thin film. The resulting electrodes were punched into discs 1.0 cm in diameter, with each disc containing approximately 15 ~ 20 mg of metal oxides. AMPIX cells[49] were constructed in an argon glovebox with lithium-metal counter-electrodes, two discs of glass fiber separators (Whatman GF/D) and 1 M lithium hexafluorophosphate ($LiPF_6$) in a solution of EC:DMC:DEC (1:1:1 by volume). XPS (Thermo Fisher Escalab 250Xi) was performed using a monochromatic Al Kα X-ray source (1486.6 eV) operating at 100 W. Micro-structural morphologies of the synthesized products was examined using field emission SEM (JEOL-6300F) and TEM (JEM 2010FEF). Elemental distribution was analyzed via EDS (Thermo Fisher Apreo 2S HiVac). SEM imaging and EDS analysis were performed at an acceleration voltage of 15 kV and a beam current of 0.4 nA. The EDS spectra were acquired over an energy range of 0.1–20 keV with a live time of 60 s to ensure robust elemental quantification. HAADF-STEM (High-angle annual dark-field scanning TEM) observations were performed using a 200 kV JEM-ARM200F (JEOL NEOARM) equipped with a spherical-aberration corrector (CEOS Gmbh). The convergence angle was chosen of 30 mrad. The annular-dark field detector inner and outer angles were 68 and 280 mrad, respectively. Raman patterns were collected using the Lab RAM HR Evolution. Although HED-Nb_2O_5 was not fully dissolved in hydrofluoric acid and aqua regia, the contents of supernatants were quantitatively determined using ICP mass spectrometry (Thermo Fisher), respectively. The distribution of elements in HED-Nb_2O_5 was analysed using time-of-flight secondary ion mass spectroscopy (ToF-SIMS 5 iontof). The powder sample was prepared for TOF-SIMS analysis by compacting it into a flat pellet to ensure a uniform surface. Prior to analysis, optional surface cleaning was conducted via pre-sputtering with a 500 eV Ar^+ ion beam for 60 s to remove potential contaminants. Both positive and negative secondary ion modes were employed under static conditions to preserve surface integrity. Charge neutralization was achieved using a low-energy electron flood gun (≤ 20 eV). EPR was performed on a EMX-plus-10/12 instrument in X-band mode with a microwave frequency of 9.48 GHz at room temperature (27 ± 1 °C). Prior to measurements, the magnetic field calibration was verified using a standard ($g = 2.0036$) to ensure accuracy. The powders of Nb_2O_5 oxides were uniformly packed into a quartz EPR tube. The magnetic field was scanned from 0 to 7000 G, centered on the resonance region of interest. Each spectrum was acquired by averaging three consecutive scans using a time constant of 20.48 ms. The g-factor is calculated using the formula:

$$g = h\upsilon/\beta H \quad (2)$$

Where, $h = 4.135 \times 10^{-15}$ eVs is the Plank constant; $\upsilon = 9.48$ GHz is the microwave frequency of X-band spectrometer; $\beta = 5.788 \times 10^{-5}$ eV T^{-1} is the electron Bohr magneton; H is the applied magnetic field.

Data availability

All data needed to evaluate the conclusions in the paper are presented in the paper. Additional data related to this paper are available from the corresponding author upon request. Source data are provided with this paper. Source Data file has been deposited in Figshare under accession code https://doi.org/10.6084/m9.figshare.28892165[50].

References

1. Neamen, D. A. *Semiconductor Physics and Devices: Basic Principles*. Ch. 4. (McGraw-Hill, New York, NY, 2012).
2. Zhang, T. et al. In situ design of advanced titanium alloy with concentration modulations by additive manufacturing. *Science* **374**, 478–482 (2021).
3. Chen, H. et al. Sub-50-ns ultrafast upconversion luminescence of a rare-earth-doped nanoparticle. *Nat. Photon.* **16**, 651–657 (2022).
4. Zhao, Y. et al. Suppressing ion migration in metal halide perovskite via interstitial doping with a trace amount of multivalent cations. *Nat. Mater.* **21**, 1396–1402 (2022).
5. Zhou, S. et al. Aspartate all-in-one doping strategy enables efficient all-perovskite tandems. *Nature* **624**, 69–73 (2023).
6. Sun, H. H. et al. Transition metal-doped Ni-rich layered cathode materials for durable Li-ion batteries. *Nat. Commun.* **12**, 6552 (2021).
7. Xie, F. et al. Progress in niobium-based oxides as anode for fast-charging Li-ion batteries. *Energy Rev.* **2**, 100027 (2023).
8. Barnes, P. et al. Electrochemically induced amorphous-to-rock-salt phase transformation in niobium oxide electrode for Li-ion batteries. *Nat. Mater.* **21**, 795–803 (2022).
9. Griffith, K. J., Wiaderek, K. M., Cibin, G., Marbella, L. E. & Grey, C. P. Niobium tungsten oxides for high-rate lithium-ion energy storage. *Nature* **559**, 556–563 (2018).
10. Augustyn, V. et al. High-rate electrochemical energy storage through Li^+ intercalation pseudocapacitance. *Nat. Mater.* **12**, 518–522 (2013).
11. Merryweather, A. J. et al. Operando monitoring of single-particle kinetic state-of-charge heterogeneities and cracking in high-rate Li-ion anodes. *Nat. Mater.* **21**, 1306–1313 (2022).
12. Sun, H. et al. Three-dimensional holey-graphene/niobia composite architectures for ultrahigh-rate energy storage. *Science* **356**, 599–604 (2017).
13. Zhu, X. et al. Zinc niobate materials: crystal structures, energy-storage capabilities and working mechanisms. *J. Mater. Chem. A* **7**, 25537–25547 (2019).
14. Lv, C., Lin, C. & Zhao, X. S. Rational design and synthesis of nickel niobium oxide with high-rate capability and cycling stability in a wide temperature range. *Adv. Energy Mater.* **12**, 2102550 (2022).
15. Cheng, C. et al. Internal and external cultivation design of zero-strain columbite-structured MNb_2O_6 toward lithium-ion capacitors as competitive anodes. *Adv. Energy Mater.* **13**, 2302107 (2023).
16. Landau, L. D. & Lifshitz, E. M. *Course of Theoretical Physics: Vol. 5, Statistical Physics*, Part 1. (Butterworth-Heinemann, 1980).
17. Anderson, P. W. More is different. *Science* **177**, 393–396 (1972).
18. Yeh, J.-W. et al. Nanostructured high-entropy alloys with multiple principal elements: novel alloy design concepts and outcomes. *Adv. Eng. Mater.* **6**, 299–303 (2004).
19. Han, L. et al. Multifunctional high-entropy materials. *Nat. Rev. Mater.* **9**, 846–865 (2024).
20. McCormack, S. J. & Navrotsky, A. Thermodynamics of high entropy oxides. *Acta Mater.* **202**, 1–21 (2021).
21. Sarkar, A. et al. High-entropy oxides: fundamental aspectsand electrochemical properties. *Adv. Mater.* **31**, 1806236 (2019).
22. Sarkar, A. et al. High entropy oxides for reversible energy storage. *Nat. Commun.* **9**, 3400 (2018).
23. Aamlid, S. S. et al. Understanding the role of entropy in high entropy oxides. *J. Am. Chem. Soc.* **145**, 5991–6006 (2023).
24. Zhang, R. et al. Compositionally complex doping for zero-strain zero-cobalt layered cathodes. *Nature* **610**, 67–73 (2022).
25. Li, T. et al. A niobium oxide with a shear structure and planar defects for high-power lithium ion batteries. *Energy Environ. Sci.* **15**, 254–264 (2022).
26. Griffith, K. J. et al. High-rate intercalation without nanostructuring in metastable Nb_2O_5 bronze phases. *J. Am. Chem. Soc.* **138**, 8888–8899 (2016).

27. Griffith, K. J. et al. Ionic and electronic conduction in $TiNb_2O_7$. *J. Am. Chem. Soc.* **141**, 16706–16725 (2019).
28. Kocer, C. P., Griffith, K. J., Grey, C. P. & Morris, J. A. Cation disorder and lithium insertion mechanism of wadsley-roth crystallographic shear phases from first principles. *J. Am. Chem. Soc.* **141**, 15121–15134 (2019).
29. Jehng, J. M. & Wachs, I. E. Structural chemistry and Raman spectra of niobium oxides. *Chem. Mater.* **3**, 100–107 (1991).
30. Skrodczky, K. et al. Niobium pentoxide nanomaterials with distorted structures as efficient acid catalysts. *Commun. Chem.* **2**, 129 (2019).
31. Brayner, R. & Bozon-Verduraz, F. Niobium pentoxide prepared by soft chemical routes: morphology, structure, defects and quantum size effect. *Phys. Chem. Chem. Phys.* **5**, 1457–1466 (2003).
32. Zhecheva, E. et al. EPR studies of Li deintercalation from $LiCoMnO_4$ spinel-type electrode active material. *J. Power Sources* **159**, 1389–1394 (2006).
33. Drouilly, C. et al. ZnO oxygen vacancies formation and filling followed by in situ photoluminescence and in situ EPR. *J. Phys. Chem. C.* **116**, 21297–21307 (2012).
34. Smirnov, A. I. et al. Magnetic resonance of intrinsic defects in the spin–Peierls magnet $CuGeO_3$. *J. Exp. Theor. Phys.* **87**, 1019 (1998).
35. Gafurov, M. R. et al. EPR study of some rare-earth ions (Dy^{3+}, Tb^{3+}, and Nd^{3+}) in $YBa_2Cu_3O_6$-compound. *J. Magn. Reson.* **161**, 210–214 (2003).
36. Muralidhara, R. S. et al. EPR and optical absorption studies of Fe^{3+} ions in sodium borophosphate glasses. *J. Phys. Chem. Solids* **71**, 1651–1655 (2010).
37. Kong, L. et al. Revisiting Li^+ intercalation into various crystalline phases of Nb_2O_5 anchored on graphene sheets as pseudocapacitive electrodes. *J. Power Sources* **309**, 42–49 (2016).
38. Xia, R. et al. Nickel niobate anodes for high rate lithium-ion batteries. *Adv. Energy Mater.* **12**, 2102972 (2022).
39. Yao, Z. et al. Smart construction of integrated CNTs/$Li_4Ti_5O_{12}$ core/shell arrays with superior high-rate performance for application in lithium-ion batteries. *Adv. Sci.* **5**, 1700786 (2018).
40. Cao, D. et al. H-Nb_2O_5 wired by tetragonal tungsten bronze related domains as high-rate anode for Li-ion batteries. *Energy Storage Mater.* **11**, 152–160 (2018).
41. Song, Z. et al. Ultrafast and stable Li-(De)intercalation in a large single crystal H-Nb_2O_5 anode via optimizing the homogeneity of electron and ion transport. *Adv. Mater.* **32**, 2001001 (2020).
42. Lim, E. et al. Facile synthesis of Nb_2O_5@carbon core-shell nanocrystals with controlled crystalline structure for high-power anodes in hybrid supercapacitors. *ACS Nano* **9**, 7497–7505 (2015).
43. Guo, B. et al. A long-life lithium-ion battery with a highly porous $TiNb_2O_7$ anode for large-scale electrical energy storage. *Energy Environ. Sci.* **7**, 2220–2226 (2014).
44. Zhou, P. et al. Solar-to-hydrogen efficiency of more than 9% in photocatalytic water splitting. *Nature* **613**, 66–70 (2023).
45. Sun, Y. et al. Bright and stable perovskite light-emitting diodes in the near-infrared range. *Nature* **615**, 830–835 (2023).
46. Yi, H. et al. Interface-induced superconductivity in magnetic topological insulators. *Science* **383**, 634–639 (2024).
47. Griffith, K. J. *Atomic and Electronic Structure of Complex Metal Oxides During Electrochemical Reaction with Lithium* (University of Cambridge, 2018).
48. Weppner, W. & Huggins, R. A. Determination of the kinetic parameters of mixed-conducting electrodes and application to the system Li_3Sb. *J. Electrochem. Soc.* **124**, 1569–1578 (1977).
49. Borkiewicz, O. J. et al. The AMPIX electrochemical cell: a versatile apparatus for in situ X-ray scattering and spectroscopic measurements. *J. Appl. Cryst.* **45**, 1261–1269 (2012).
50. Xu, J. High-entropy-doping effect in a rapid-charging Nb2O5 lithium-ion battery negative electrode. *Figshare* https://doi.org/10.6084/m9.figshare.28892165 (2025).

Acknowledgements

J.X. thanks the funding support from Open Fund of Key Laboratory of Advanced Energy Materials Chemistry, Ministry of Education (Nankai University), "Regional Joint Fund - Youth Fund Project"(Grant No. 2023A1515110099) from Department of Science and Technology of Guangdong Province, "Hundred Young Talents Program" (Grant No. 263113491) from Guangdong University of Technology and "2023 Annual Basic and Applied Basic Research Topic" (Grant No. 2023A04J1600) from Guangzhou Municipal Science and Technology Bureau. L.T. acknowledges support by the National Key Research and Development Program of China (Grant No. 2023YFB3208002), National Natural Science Foundation of China (Grant No. 62005051), Key Laboratory of Photoelectric Imaging Technology and System (MOE), and Analysis & Testing Center of Beijing Institute of Technology.

Author contributions

J.X. conceived the idea and designed the experiments. J.X., Y.W., and Z.S. supervised the project and provide the support. J.X., F.X., and L.H. fabricated the materials, performed electrochemical measurements, and analyzed the data. J.X., N.L., and F.X. performed the crystal structural analysis. J.X., S.P., F.X., Y.W,. and W.M. performed the microscopic observation. J.X., Y.W., and Z.S. discussed the design of experiment with L.S., X.S., J.C., L.T., K.Z. (HPSTAR), K.Z. (NKU), and Z.Z. J.X. wrote the paper with input from the all other authors.

Competing interests

The authors declare no competing interests.

Additional information

Supplementary information The online version contains supplementary material available at https://doi.org/10.1038/s41467-025-60186-6.

Correspondence and requests for materials should be addressed to Junling Xu, Yonggang Wang or Zhipeng Sun.

Peer review information *Nature Communications* thanks the anonymous reviewers for their contribution to the peer review of this work. A peer review file is available.